The Intrinsic Ability of Silk Fibroin to Direct the Formation of Diverse Aragonite Aggregates

*Ting Wang, David Porter, and Zhengzhong Shao**

As an analogue of the main protein contained in naturally formed nacre, reconstituted silk fibroin (SF) from the *Bombyx mori* silkworm silk shows a strong preference for the formation of the aragonite form of $CaCO_3$ crystals and allows fine control over their size and morphology. The aragonite phase could be generated via two different routes: direct growth or dissolution and recrystallization, depending on the concentration of Ca^{2+} and SF. Generally, lower concentrations of Ca^{2+} and SF favor the formation of aragonite needles and their aggregates, of which the lattice structure of the precursor is similar to that of the organic matrix in natural shell. Higher concentrations lead to the formation of aragonite aggregates via a dissolution and recrystallization process through intermediates of lens-like vaterite. Molecular modeling shows that the β-strand conformers of silk fibroin molecules has an excellent match with the ionic spacing in the aragonite (010) plane, which can promote growth along the (001) long axis of aragonite crystals. This synergy between silk fibroin and the aragonite phase may help our understanding of the function of organic matrices involved in the biomineralization process, and facilitate the fabrication of synthetic materials with the potential for high performance mechanical properties.

1. Introduction

The biomineralization process provides unique inspiration for materials design, as illustrated by the mechanical properties of many biominerals achieved through their superior hierarchical organization relative to synthetic materials.[1] Living organisms are capable of developing complicated architectures with combinations of organic and inorganic components to fulfill important biological functions, such as bones for skeletal support and shells for the protection of soft tissues.[1] The organic matrices, usually consisting of proteins and polysaccharides, are minority components compared with inorganic minerals, and the low concentration (ranging from 2% to 5% in common biomaterials)[2,3] also implies a high efficiency of mineral-associated macromolecules in the fabrication of biominerals with excellent properties.

Mollusk shell nacre, one of the most studied biominerals, is renowned for its remarkable mechanical features because of its highly regular "brick-and-mortar" arrangement.[1] The formation of biogenic aragonite crystals is subject to the network of oriented biomacromolecules at the early stage of biomineralization.[4] It has been reported that β-chitin, one of the main components of the organic matrix in nacreous tablets, acts as the framework for the entire construction and is preferentially oriented parallel to the *a*-axis of aragonite tablets;[2,5] however, its lack of functional groups (i.e., carboxylates) capable of strong interaction with $CaCO_3$ reduces its contribution to the control over the polymorph and orientation of minerals.[6,7] Several studies have reported the formation of aragonite *in vitro* using proteins extracted from nacre in the absence of chitin.[8,9] Therefore, proteins in nacreous tablets – so-called "silk-fibroin-like proteins" and acid glycoproteins – may play an important role in regulating the morphology and lattice structure of $CaCO_3$ minerals through such factors as the protein sequence, active functional groups and conformation.[7,10] These matrix proteins are believed to interact both with β-chitin fibrils and growing crystals so as to translate the orientation of chitin to the minerals.[6] Numerous efforts have been undertaken to identify and characterize the matrix proteins present in the nacreous tables[2,7,11,12] and to mimic the growth process of aragonite minerals in vitro through the involvement of various natural and synthesized additives.[13–17] However, this process remains elusive due to the fact that it is difficult to investigate the molecular-level interaction between proteins and minerals, and to understand the importance of protein sequences and conformation in controlling the structure of biominerals, as well as the role of other possible proteins involved in the bimineralization process.[14,18]

In recent years, many studies have been focused on the synthesis of aragonite crystals or hierarchical particles with laminated structures,[16,19] and most were performed through the application of organic matrix extracted from natural nacreous

Dr. T. Wang, Prof. Z. Shao
Key Laboratory of Molecular Engineering of Polymers of Ministry of Education
Advanced Materials Laboratory
Department of Macromolecular Science
Fudan University
Shanghai 200433, P. R. China
E-mail: zzshao@fudan.edu.cn
Dr. D. Porter
Department of Zoology
University of Oxford
South Parks Road, Oxford OX1 3PS, UK

DOI: 10.1002/adfm.201101011

tablets[8,14,18,20] or under particular ambient environments.[21–24] However, silk fibroin (SF, one of the analogues of silk-fibroin-like protein), derived from silkworm silk of *Bombyx mori* exhibited a high preference for the aragonite form of $CaCO_3$ in a series of our experiments, even in a system with relatively high crystallization rate (during the ripening process),[25,26] as the acidic amino acid residues on it played the role of nucleation while the conformation of it mediated the polymorph of $CaCO_3$. Here, we present a detailed investigation into the role of SF in an aqueous environment acting on the growth of $CaCO_3$ at extremely slow crystallization speeds (in a CO_2 vapor diffusion system, which is a good method to investigate the interaction between additives and minerals)[27] and to show the deposition of diverse aragonite crystals over a wide concentration range of silk fibroin (0.01 to 2 wt-%). Interestingly, we observed a continuous change in the morphology and structural forms of the final aragonite products using different concentrations or different growth pathways as a consequence of the complex regulation between thermodynamic and kinetic factors in the crystallization process. SF also appears to show a strong preference for the formation of aragonite phase due to the stereochemical matching of protein and mineral phases.

2. Results and Discussion

2.1. The Morphology Evolution of Aragonite/SF Hybrids by Regulating Component Concentration

A remarkable dependence of the crystal morphology on the concentration of the components, i.e., Ca^{2+} and SF, at a certain mass ratio of $[Ca^{2+}]$:[SF] was observed and representative images of $CaCO_3$/SF hybrid are shown in **Figure 1**. For $[Ca^{2+}]$:[SF] = 1:1, a low component (either SF or Ca^{2+}) concentration (0.01%) yielded aggregates (13–17 μm in size, shown in Figure S1a in the Supporting Information) with loosely packed layered needle-like units (Figure 1a). The aragonite structure was confirmed by both Raman spectroscopy[28,29] on individual crystals and also XRD measurement of the entire sample, which corresponded to a pure aragonite phase (Raman and XRD spectra of representative crystals are presented in Figures S2 and S3). Needles with sizes of 50–100 nm were aligned along the longitudinal axis direction of the aragonite bundles, and the crystal faces were quite smooth and defect-free (Figure S4). A complete transition of the morphology of the aggregate was achieved with SF concentrations ranging from 0.1% to 0.5%. At [SF] = 0.1%, a uniform population of aragonite aggregates around 8 μm in length (Figure S1b) exhibited a shuttle-like profile and similarly layered structure of aligned needles (Figure 1b). When the concentration of SF was increased to 0.5%, some differences in the crystal aggregates were observed. The surface of such 5 μm shuttle-like aggregates (Figure S1c) appeared to be granular and rough, comprising bricks with varying size (Figure 1c). Higher concentration ([SF] = 1%) further enhanced this effect, producing 4 μm crystals (Figure S1d) consisting of irregular and smaller aragonite particles which still kept the orientation along the long axis of the aggregates (Figure 1d). A typical morphology produced at [SF] = 2% is shown in Figure 1e. Ellipsoidal aggregates with size of 3 μm, consisting of densely packed particles, oriented along the long axis of the particles (Figure S1e). Figure 1f shows the gradual decrease in size with increasing SF concentration, implying a barrier to crystal growth by SF in the long-axis.

Decreasing the $[Ca^{2+}]$ and [SF] mass ratio to 1:5 yielded a similar pattern of morphology changes as observed at $[Ca^{2+}]$:[SF] = 1:1 with varied component (either SF or Ca^{2+}) concentration. Initially, 500 nm aragonite needles were obtained with smooth crystal faces at [SF] = 0.1%, and some of the area on the surface displayed the fusion signs of smaller units (Figure S5a). Increasing the SF concentration to 0.5% produced needle aggregates with irregular profile (Figure S5b). In common with the morphology modification observed before,

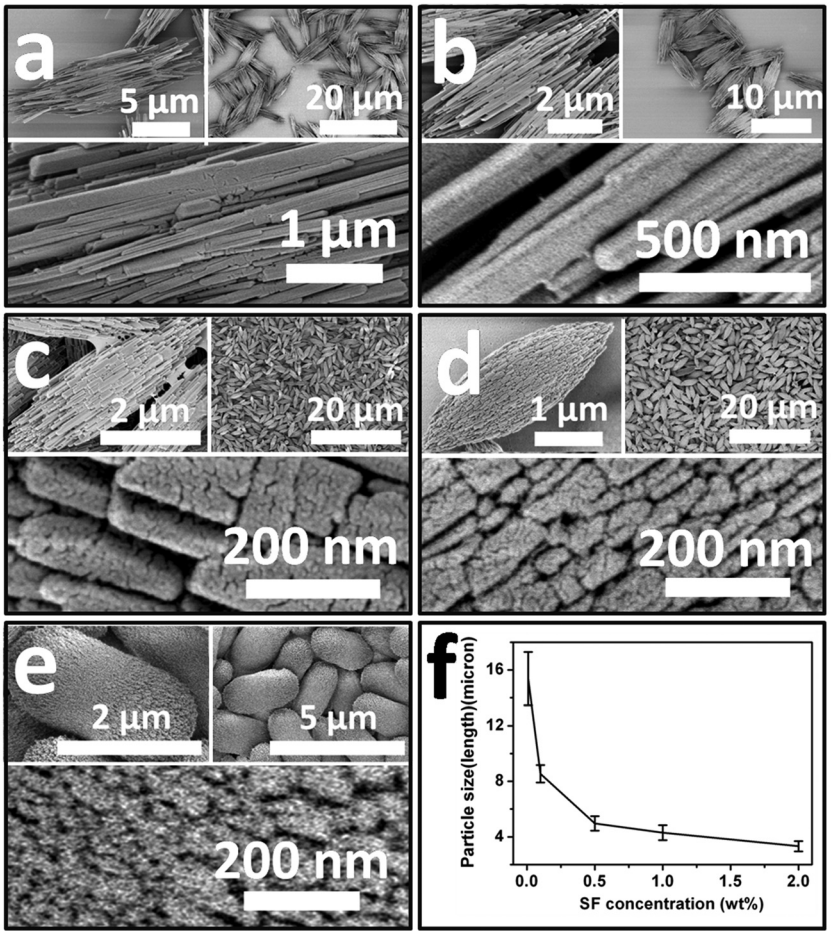

Figure 1. FE-SEM images of the aragonite crystals obtained after 48 h from a solution containing SF and Ca^{2+} at a fixed $[Ca^{2+}]$:[SF] mass ratio of 1:1 and SF concentration of: a) 0.01%; b) 0.1%; c) 0.5%; d) 1%, and, e) 2%. The insets show larger scale panoramic views of the structures. f) The size change of crystals with increasing concentration of SF.

higher component concentration led to gradual structural evolution from obvious needle aggregates (Figure S5c) to aragonite bundles with enhanced surface roughness constructed from small, distinct crystalline units (Figure S5d).

Due to the strong dependence of the particle structure and morphology on the Ca^{2+} concentration, a series of experiments was performed to investigate the effects of the Ca^{2+} concentration at a constant SF concentration of 0.2% (**Figure 2**). At [Ca^{2+}]:[SF] = 1:10, aragonite needles with relatively uniform size (both in length and width) were produced (Figure 2a). Higher Ca^{2+} concentrations contributed to an aggregation trend of needle-like units. The arrangement of these aragonite units varied from slightly grouped (Figure 2b) to loosely aligned (Figure 2c), and further changed into tightly packed (Figure 2d). However, there seemed to be little change in size with increasing Ca^{2+} concentration.

In the above series, increasing Ca^{2+} concentration induces the morphology transition from individual needles to bundles of needles, without significant changes in the needle size. The morphology of hybrids shown in Figure 2, however, was accompanied by increasing surface roughness and reducing unit size along with gradual increase of component concentration. Basically, increasing SF concentration could enhance the opportunity for heterogeneous nucleation on the SF chains or more SF chains would join the crystallization process (inhibition or stabilizing) to further realize the modification and control of silk fibroin over the morphology of final hybrids.

2.2. The Growth Pathway of Aragonite/SF Hybrids with Different Component Concentration

SF was extremely versatile in its control over the structure of aragonite crystals, depending on component concentration. Different concentrations of SF and Ca^{2+} led mainly to three kinds of crystal structure: needles, needle bundles and particle-packed aggregates, along with increasing surface roughness. The growth pathway of individual kinds of aragonite crystals was examined to further investigate the effect of SF in the crystallization process of $CaCO_3$. Based on our experiments, the aragonite crystals were generated primarily via direct growth (**Figure 3**) or dissolution and recrystallization (Figure S6), as summarized in **Table 1**.

Aragonite crystals could be produced with relatively low concentrations of Ca^{2+} and SF in the form of needles and needle aggregates (displayed in the areas with low and medium grey levels in Table 1). The growth process of such crystals is shown in Figure 3. Initially, the image of the original sample indicated a liquid-like substance (Figure 3a), and the corresponding EDX spectrum (inserted in the left of Figure 3a) demonstrated that the selected area was mainly composed of Ca, O, and C. The obvious dispersion ring of electron diffraction (ED) reflected that the formed $CaCO_3$ was in the amorphous phase. In the course of time, a gradual crystallization process was observed. After 2 h, the material maintained its liquid-like properties but, surprisingly, localized areas showed aligned parallel striations, with these lattice lines separated from each other by about 2–4 nm (Figure 3b). The lattice structure became more obvious and spread to the entire aragonite precursor after 4 h (Figure 3c), and the transient precursor presented a ribbon-like shape, slightly overlapping and interlocking in the dense network (Figure S7a). ED patterns, meanwhile, confirmed that the aragonite phase was formed, although the pattern is not indexed (inset in Figure 3c). Interestingly, the organic matrix in natural *bivalve mollusk* exhibited exactly the above lattice structure (Figure S7b),[2] which afforded important information for the investigation of the relationship between aragonite phase and silk fibroin. With reaction time increasing to 6 h, a number of aragonite nanoneedle units (around 5 nm) were detected in the form of aggregates in packets with varied size (30–100 nm) (Figure 3d and Figure S7b). After 12 h, fully developed aragonite crystals (needles and needle bundles) were observed (Figure 3e and Figure 3g). For those of needles (as well as the aggregates formed by the needles), each one showed a well-defined characteristic of single crystal viewed along the [010] direction as demonstrated by ED (the inset in Figure 3e and Figure 3g, respectively). Also the above ED results as well as HRTEM images (Figure 3f and Figure 3h) showed that the long axis of the needle was [001]. Moreover, few examples of individual aragonite needles (around 30–50 nm) were observed, since these needle units preferred to aggregate into bundles, especially with higher concentrations with a higher density of nucleation points.

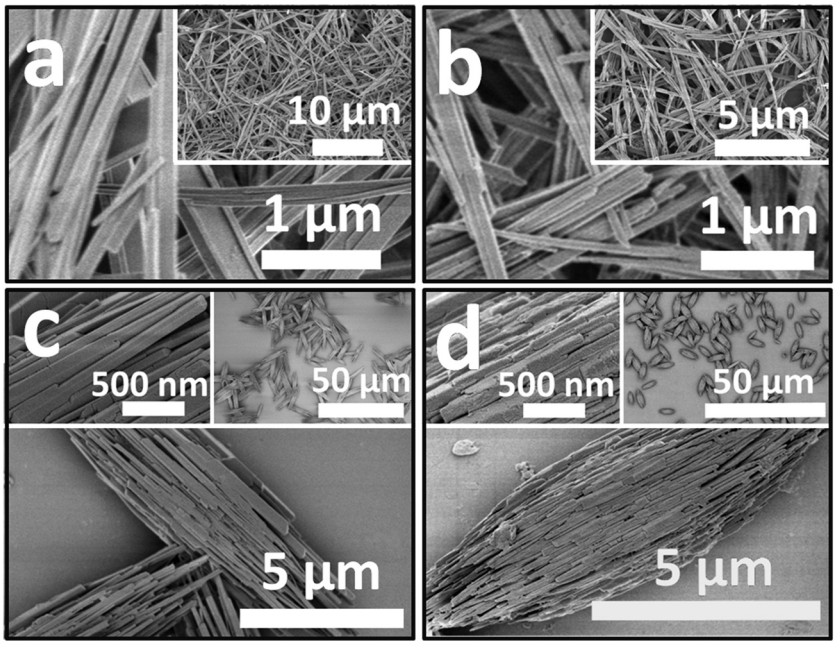

Figure 2. FE-SEM images of the aragonite crystals precipitated after 48 h from a solution containing 0.2% silk fibroin and with different [Ca^{2+}]:[SF] mass ratio: a) 1:10; b) 1:5; c) 1:1; and, d) 10:1. Insets show structural details (left) and panoramic images of each sample (right).

As mentioned above, the aligned parallel structure of aragonite precursor (Figure 3c) was very similar to the organization of the organic matrix in natural shell,

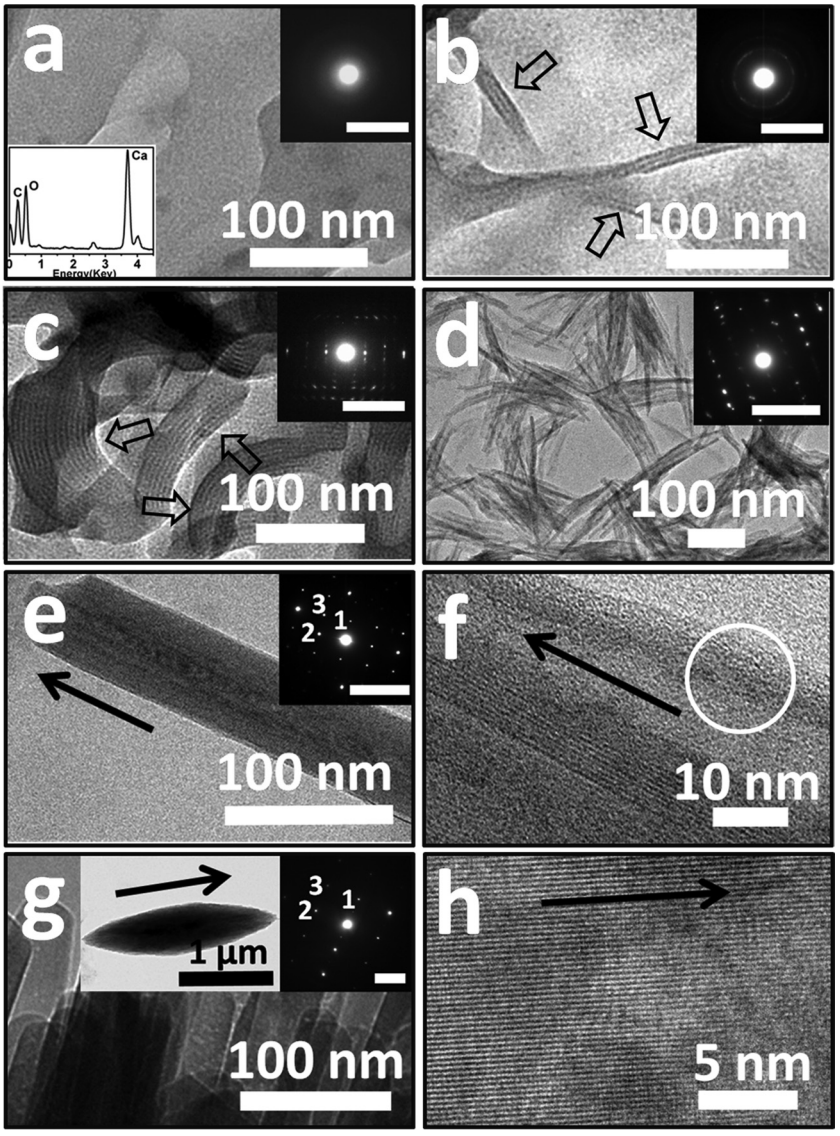

Figure 3. TEM images of the formation process of aragonite crystals via direct growth: a) 5 min; b) 2 h; c) 4 h; d) 6 h; e) 12 h; and, g) 12 h. The inset in (a) shows the EDX spectrum of early substances. Other insets indicate the corresponding evolution process of ED patterns. Scale bar, 5 nm^{-1}. f,h) HRTEM images of the aragonite needle (e) and aggregate (g). The ED patterns and HRTEM images of (e) and (g) indicate the orientation along the [010] zone axis, showing as 1 = (001), 2 = (100), 3 = (101). The open arrows indicate the aligned parallel striations on the precursor of aragonite crystals. The black arrows show [001] direction along the long axis of the crystals. The parameters of the crystal are referenced to (76-0606).

which contributed to the formation of its hierarchical structure.[1] It is worth noting that SF (*Bombyx mori* silk) can be made to fold into regular β-sheets and self-assemble to nanofibrils spontaneously in an aqueous environment.[30,31] Hence, it could be speculated that such parallel linear structures of aragonite precursor might correspond to the β-sheet conformation and assembly of SF chains, which act as a template for aragonite phase and further promote the generation of aragonite nanoneedle aggregates of the same size (around 50 nm) via rapid dehydration and crystallization.

The concept of "short-range order" has been associated with early periods of prenucleation and precursor stages,[32,33] so the polymorph could be determined at the very beginning of the crystallization process. For the selection between calcite and aragonite forms, our experimental results suggested that control of SF in the earlier phases was highly significant, and our extensive experience with silk molecular structures suggested that silk β-sheets would most likely contribute to the preferential growth of aragonite crystals. Such a process would, presumably, be related to stereochemical recognition or interaction between the β-sheet conformation and the aragonite morphology. Therefore, molecular modeling was used to examine the relationship between the protein β-sheet conformation (β-strand) and specific crystalline faces.

For clarity here, a tetrapeptide segment of a β-strand poly(glycine) chain was compared with the atomic structure of the different $CaCO_3$ crystal faces, which were obtained by cleaving lattice models of the different $CaCO_3$ polymorphs, as shown in **Figure 4** and Figure S8. For purposes of a simple comparison, the atomic positions in the individual peptide segments and $CaCO_3$ crystal faces were fixed in their minimum energy positions, and then searches were made for minimum energy adsorption matches of the peptide on the crystal faces. Since the polar amide groups of the protein chain backbone have the strongest interaction with the inorganic ions, we found little difference in our simulations between the simple poly(glycine) chains and the SF characteristic sequence of –Gly–Ala–Gly–Ala–Gly–Ser–. The simulations established that there is an excellent match between the ionic spacing in the aragonite (010) plane and the silk β-sheet lattice (Figure 4), while other crystal faces of aragonite have poor matches. The (010) face is the main slow growth face in aragonite which is perpendicular to the direction with high growth rate along the (001) long axis of the crystal. Therefore, the β-strands of silk chain parallel to the long axis could optimally absorb onto the (010) face to promote aragonite long-axis growth towards the (001) direction. Furthermore, the β-strand of $(Gly)_4$ was compared with the three main faces of the thermodynamically more stable calcite crystals, i.e., (100), (010), and (001). The simulations showed that the β-strand could not find a good energy-minimum position on any of the crystal faces specifically (Figure S8). Lacking any specific nucleation or inhibition preferences for calcite crystal faces resulted in a crystallization path favoring the formation of aragonite.

Aragonite aggregates with merged-particle structures could be obtained via a dissolution and recrystallization pathway, mainly under conditions of high component concentration

Table 1. Morphology and crystallization pathway of aragonite crystals obtained at different Ca^{2+} and SF concentrations.

Concentration of SF	Morphology and polymorph of final products and crystallization pathway at different $[Ca^{2+}]$:[SF]						
[wt-%]	1:10	1:5	1:2	1:1	10:1	50:1	100:1
0.01	–[c]	–[c]	–[c]	[NA][a]	[NA][a]	[NA][b]	[PA][b]
0.05	–[c]	–[c]	–[c]	[NA][a]	[NA][a]	[PA][b]	[PA][b]
0.1	–[c]	[N][a]	[NA][a]	[NA][a]	[PA][b]	[PA][b]	[PA][b]
0.2	[N][a]	[NA][a]	[NA][a]	[NA][a]	[PA][b]	[PA][b]	[PA][b]
0.5	[NA][a]	[NA][a]	[PA][b]	[PA][b]	[PA][b]	–[d]	–[d]
1	[PA][b]	[PA][b]	[PA][b]	[PA][b]	[PA][b]	–[d]	–[d]
2	[PA][b]	[PA][b]	[PA][b]	[PA][b]	–[d]	–[d]	–[d]

[a]The aragonite particles were produced via direct growth; [b]These aragonite aggregates were deposited through dissolution and recrystallization pathway; [c]Extremely low concentration of substances hardly induced nucleation; [d]High concentration of SF and Ca^{2+} (the concentration of SF was beyond 0.5% and $[Ca^{2+}]$ was more than 20 mmol L^{-1} at the same time in our experiment.) led to salting-out, which cannot realize mediation; [N] Individual needles; [NA] Needle aggregates; [PA] Aggregates consisting of brick-like or irregular particles.

(exhibited in area with darker grey level in Table 1). Spherical precursor nanoparticles (around 30 nm in size) with rough profile and no obvious boundaries formed after 2 h reaction. Subsequent aggregation resulted in the deposition of lens-like vaterite with a size of around 5 μm after 12 h. In the course of time, the vaterite phase dissolved gradually and continuously to produce more stable aragonite crystals (Figures S6c and S6d). The final product was scattered as "single crystals" which had the same orientation along the [001] direction as the aragonite needles discussed above (inset in Figure S6d). Clearly, for the recrystallization of vaterite aggregates, which was thermodynamically controlled, the polymorph switching of final product

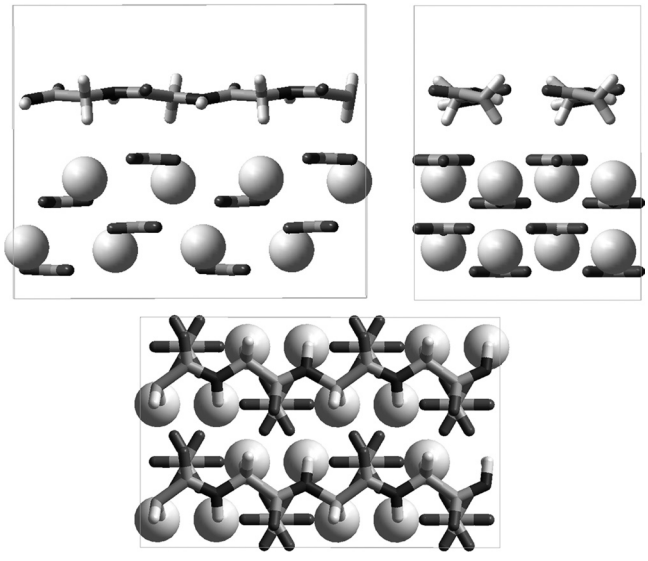

Figure 4. Modeling of the matching of silk β-sheet and the aragonite (010) face. The three views are from different directions with β-strand backbone chain, calcium ion spheres and star-shaped carbonate ions.

also followed stereochemical recognition with β-sheets of SF to prefer the aragonite phase.

Crystal growth is generally considered either by classical ion-by-ion addition or via an aggregation-based route.[24,34] Based on our results, the aggregation process produced various aragonites, from single needles to particle-packed aggregates with increasing concentration of both components, depending on the selection of crystallization pathways (direct growth or dissolution and recrystallization), as well as the structure and polymorph of the crystalline precursor. For example, the crystallization route showed a gradual transition from direct aragonite growth to dissolution and recrystallization when increasing $[Ca^{2+}]$:[SF] at a fixed SF concentration (shown in Table 1). On the other hand, the initial polymorph selection between aragonite and vaterite phase depended on the Ca^{2+} and SF concentration. We need to bear in mind the solubility product (K_{sp}) of different polymorphs, that is $-\log K_{sp}^{25\ °C}$: ACC = 6.4, vaterite = 7.91, aragonite = 8.34, and calcite = 8.48.[1,24] The extremely low Ca^{2+} concentration (e.g., $[Ca^{2+}]$ = 0.01–0.1 mM) cannot reach or just reaches the critical nucleation point (the involvement of SF contributes to increasing the local supersaturation), which results in the development of crystallization that is controlled by the thermodynamic equilibrium to form an aragonite phase (Figure 1a, 2a, 2b, and S5a) until the precursor is completely consumed. On the other hand, high Ca^{2+} concentration (far away from the solubility equilibrium values, 0.2 mM or even higher in our cases) would induce kinetically controlled reaction to form vaterite phase, which would also dissolve and recrystallize into the final aragonite phase. Therefore, the supersaturation extent could decide the crystallization pathway as well as the individual precursor, as shown in Figure 3 (aragonite) and Figure S6 (vaterite), respectively.

Our proposed mechanism for calcium carbonate crystallization in the presence of SF is summarized in **Scheme 1**. SF can induce the formation of aragonite crystals mainly via two routes, depending on the supersaturation, that is Ca^{2+} and SF concentration. Generally, lower concentrations of ($[Ca^{2+}]$ and [SF]) contributed to an aragonite precursor with a lattice structure (owing to the control of silk β-sheet over nucleation and prior crystallization period), which could directly produce aragonite needles as well as needle bundles via dehydration and aggregation. On the other hand, higher concentrations induced the formation of aragonite particle aggregates with lens-like vaterite intermediates via the dissolution and recrystallization route.

Thermogravimetric analysis (TGA) of carefully washed samples found SF in all these aragonite deposits. For comparison, experimental conditions with constant $[Ca^{2+}]$ and varied [SF] would lead to a relatively constant weight loss of around 5% from the final products, while fixed [SF] but differences in $[Ca^{2+}]$ resulted in increasing organic content in the final products with increasing Ca^{2+} concentration (from 3% to 5%) (Figure S9). Thus, results obtained from TGA measurements supported the mechanism we assumed above to a certain extent. SF indeed acts as a heterogenous nucleator to promote the aragonite growth because of relatively high SF content in aragonite hybrids. However, the amount of SF involved in the crystal growth process is not affected by the crystallization pathway at a constant initial Ca^{2+} concentration.

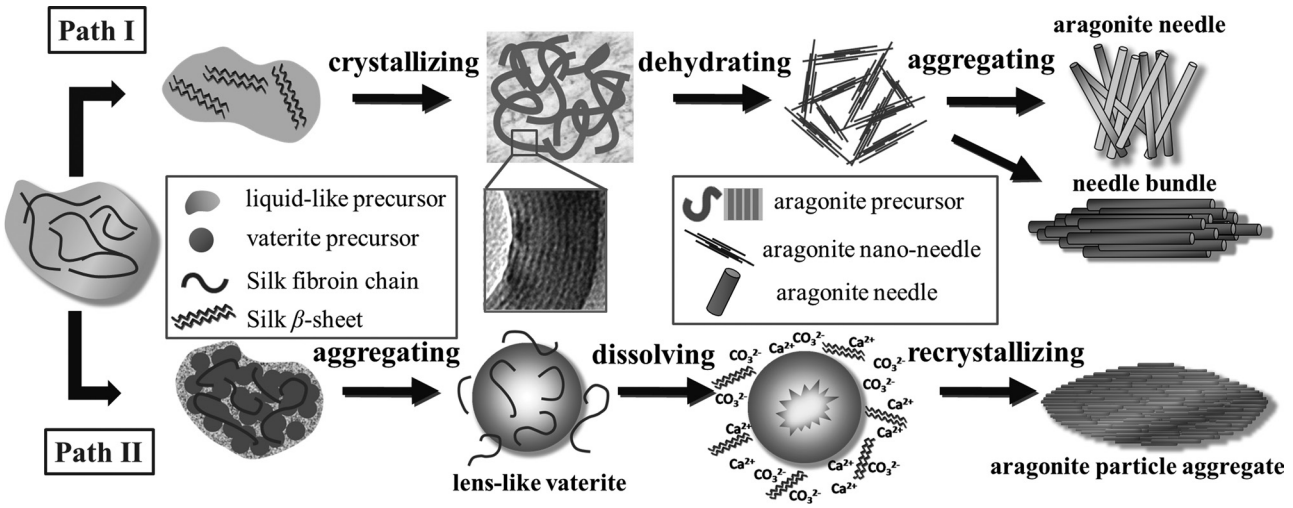

Scheme 1. Two growth pathways of aragonite crystals mediated by silk fibroin. **Path I** direct aragonite growth (low concentration); **Path II** dissolution and recrystallization (high concentration).

3. Conclusions

In general, silk fibroin gave precise control over the formation and morphology modification of aragonite single crystals over all concentrations of the components. The selection of crystallization path and precursor showed strong dependence on component concentration (supersaturation). Lower concentrations of ([Ca^{2+}] and [SF]) led to direct growth of aragonite needles via aggregation, and aragonite precursor with a lattice structure showed exactly the same profile as the organic matrix in natural shell. On the other hand, higher concentrations induced the formation of aragonite particle aggregates via dissolution and recrystallization, with lens-like vaterite as intermediate. Moreover, molecular modeling confirmed that the β-strand conformation of SF molecular chains has an excellent match to the ionic spacing in the aragonite (010) plane. So silk fibroin influenced the growth of $CaCO_3$ crystals through the absorption of β-sheet onto the aragonite (010) face, resulting in preferred growth along the (001) long axis of the crystal to promote the formation of the aragonite phase, while poor matching with SF β-sheet led to the inhibition of the calcite phase. During the slow growth of natural shell as a long-term thermodynamic process, organic components at extremely low levels favor the formation of aragonite tablets. In this work, switching between kinetic and thermodynamic factors (concentration-oriented) indicates that, similar to natural shell growth, the thermodynamic environment (i.e., the direct aragonite growth or dissolution and recrystallization process) results in the deposition of aragonite phase with the assistance of SF. Therefore, this work successfully demonstrates the control of silk fibroin over the formation of the aragonite phase with various morphologies, which provide a better understanding on the origins of aragonite formation and the function of the silk-fibroin-like protein involved in the natural biominerallization process. On the basis of this, the combination of aragonite and silk fibroin could yield new starting point for the fabrication of hybrid material with mechanical property through adopting appropriate assembly pathway.

4. Experimental Section

Materials and Preparation of Regenerated SF: A naturally spun silkworm silk fiber contains two silk fibroin core threads surrounded by a glue-like sericin coating, and the fibroin is insoluble protein containing up to 90% of amino acids of glycine (G), alanine (A), and serine (S) primarily in the repeated GAGAGS amino acid motif which leads to antiparallel β-sheet formation in fibers.[35] The degumming and dissolving process of *Bombyx mori* silk fiber followed established procedures.[25] A semi-permeable membrane (MEMBRA-CEL, 12000–14000 MWCO) was used for dialysis. The dialyzed SF aqueous solution was centrifuged at 6000 rpm for about 5 min and the supernatant, which was about 4% (w/w) of aqueous regenerated silk fibroin (SF), was collected at room temperature and stored at 4 °C.

Crystallization of $CaCO_3$: Small pieces of glass substrates were cleaned and subjected to ultrasound in a bath containing ethanol for 10 min, further soaked with a H_2O-HNO_3(65 wt-%)–H_2O_2 (1:1:1, v/v/v) solution, then rinsed with deionized water and acetone, and finally dried in air.

Crystallization was carried out in the presence of an appropriate amount of silk fibroin solution in the range of 0.01 to 2.0 wt-% via the CO_2 vapor diffusion method (modified from a classical procedure).[27] The Ca^{2+} concentration was adjusted to a certain [Ca^{2+}] and [SF] mass ratio (1:10 to 100:1). A piece of cleaned glass slide (with or without copper grid laid on) was carefully put at the bottom of the beaker containing as-prepared mixture solution (10 mL) to collect precipitates. The beaker covered by parafilm with six pinholes was transferred into a large close desiccator (about 6.5 L) as soon as possible. 15 g of crushed ammonium carbonate in another small beaker covering with parafilm with 6 pinholes was placed into the desiccator for diffusion of CO_2. The mineralization was performed at room temperature (around 25 °C). After different reaction times, the glass slide with deposits was gently rinsed by DIW and dried in vacuum overnight for further characterization.

Characterization: Scanning electron microscopy (SEM) was performed on a TS 5136MM microscope at a 20 kV acceleration voltage and Hitachi-S-4800 FE-SEM (Pt-coated prior to examination). Transmission electron microscopy (TEM)/high-resolution transmission electron microscopy (HRTEM) images and selective area electron diffraction (SAED) patterns were obtained on a JEM-2100F. Electron diffraction (EDX) was employed to determine elementary composition. The polymorph of $CaCO_3$ was determined by Renishaw inVia Reflex Raman spectrometer equipped with 633 nm Helium/Neon laser, CCD detector, and Leica 2500 optical microscopy. X-ray powder diffraction (XRD) data were recorded on an X'pert Pro with Cu Ka radiation. The sections of particles were prepared by Gatan Model 691 precision ion polishing system.

Thermogravimetric analysis (TGA) was performed at 10 K min^{-1} on DTG-60H under nitrogen gas with flow rate of 40 cm^3 min^{-1}. Molecular modeling was performed with the Cerius2 suite of programs using standard $CaCO_3$ crystal structures and β-sheet protein conformers.

Supporting Information

Supporting Information is available from the Wiley Online Library or from the author.

Acknowledgements

This work was supported by the National Natural Science Foundation of China (NSFC 20974024 and 21034003) and 973 Project of Chinese Ministry of Science and Technology (No. 2009CB930000). D.P. is supported by the European Research Council (SP2-GA-02008-233409).

Received: May 6, 2011
Revised: July 18, 2011
Published online: November 9, 2011

[1] S. Mann, *Biomineralization Principles and Concepts in Bioinorganic Materials Chemistry*, Oxford University Press, New York **2001**, pp. 1–5.
[2] Y. Levi-Kalisman, G. Falini, L. Addadi, S. Weiner, *J. Struct. Biol.* **2001**, *135*, 8–17.
[3] V. Pipich, M. Balz, S. E. Wolf, W. Tremel, D. Schwahn, *J. Am. Chem. Soc.* **2008**, *130*, 6879–6892.
[4] B. Pokroy, A. N. Fitch, E. Zolotoyabko, *Cryst. Growth Des.* **2007**, *7*, 1580–1583.
[5] L. Addadi, D. Joester, F. Nudelman, S. Weiner, *Chem. Eur. J.* **2006**, *12*, 981–987.
[6] E. C. Keene, J. S. Evans, L. A. Estroff, *Cryst. Growth Des.* **2010**, *10*, 1383–1389.
[7] S. Weiner, W. Traub, *FEBS Lett.* **1980**, *111*, 311–316.
[8] A. M. Belcher, X. H. Wu, R. J. Christensen, P. K. Hansma, G. D. Stucky, D. E. Morse, *Nature* **1996**, *381*, 56–58.
[9] T. Samata, N. Hayashi, M. Kono, K. Hasegawa, C. Horita, S. Akera, *FEBS Lett.* **1999**, *462*, 225–229.
[10] S. Sudo, T. Fujikawa, T. Nagakura, T. Ohkubo, K. Sakaguchi, M. Tanaka, K. Nakashima, T. Takahashi, *Nature* **1997**, *387*, 563–564.
[11] L. Addadi, S. Weiner, *Proc. Natl. Acad. Sci. U.S.A.* **1985**, *82*, 4110–4114.
[12] S. Weiner, W. Traub, *Philos. Trans. R. Soc. London, Ser. B* **1984**, *304*, 425–434.
[13] S. F. Chen, J. H. Zhu, J. Jiang, G. B. Cai, S. H. Yu, *Adv. Mater.* **2010**, *22*, 540–545.
[14] G. Falini, S. Albeck, S. Weiner, L. Addadi, *Science* **1996**, *271*, 67–69.
[15] B. X. Leng, F. G. Jiang, K. B. Lu, W. H. Ming, Z. Z. Shao, *CrystEngComm* **2010**, *12*, 730–736.
[16] T. Wang, B. X. Leng, R. C. Che, Z. Z. Shao, *Langmuir* **2010**, *26*, 13385–13392.
[17] S. H. Yu, H. Colfen, *J. Mater. Chem.* **2004**, *14*, 2124–2147.
[18] R. A. Metzler, J. S. Evans, C. E. Killian, D. Zhou, T. H. Churchill, N. P. Appathurai, S. N. Coppersmith, P. U. P. A. Gilbert, *J. Am. Chem. Soc.* **2010**, *132*, 6329–6334.
[19] H. Wei, N. Ma, F. Shi, Z. Q. Wang, X. Zhang, *Chem. Mater.* **2007**, *19*, 1974–1978.
[20] Q. L. Feng, G. Pu, Y. Pei, F. Z. Cui, H. D. Li, T. N. Kim, *J. Cryst. Growth* **2000**, *216*, 459–465.
[21] S. F. Chen, S. H. Yu, J. Jiang, F. Q. Li, Y. K. Liu, *Chem. Mater.* **2006**, *18*, 115–122.
[22] E. M. Flaten, M. Seiersten, J. P. Andreassen, *J. Cryst. Growth* **2009**, *311*, 3533–3538.
[23] A. Sarkar, S. Mahapatra, *Cryst. Growth Des.* **2010**, *10*, 2129–2135.
[24] A. W. Xu, W. F. Dong, M. Antonietti, H. Colfen, *Adv. Funct. Mater.* **2008**, *18*, 1307–1313.
[25] C. Cheng, Z. Z. Shao, F. Vollrath, *Adv. Funct. Mater.* **2008**, *18*, 2172–2179.
[26] T. Wang, R. C. Che, W. T. Li, R. X. Mi, Z. Z. Shao, *Cryst. Growth Des.* **2011**, *11*, 2164–2171.
[27] S. Albeck, S. Weiner, L. Addadi, *Chem. Eur. J.* **1996**, *2*, 278–284.
[28] R. G. Herman, C. E. Bogdan, A. J. Sommer, D. R. Simpson, *Appl. Spectrosc.* **1987**, *41*, 437–440.
[29] C. G. Kontoyannis, N. V. Vagenas, *Analyst* **2000**, *125*, 251–255.
[30] Z. G. Gong, L. Huang, Y. H. Yang, X. Chen, Z. Z. Shao, *Chem. Commun.* **2009**, 7506–7508.
[31] G. Y. Li, P. Zhou, Z. Z. Shao, X. Xie, X. Chen, H. H. Wang, L. J. Chunyu, T. Y. Yu, *Eur. J. Biochem.* **2001**, *268*, 6600–6606.
[32] D. Gebauer, H. Colfen, A. Verch, M. Antonietti, *Adv. Mater.* **2009**, *21*, 435–439.
[33] D. Gebauer, A. Volkel, H. Colfen, *Science* **2008**, *322*, 1819–1822.
[34] A. N. Kulak, P. Iddon, Y. T. Li, S. P. Armes, H. Colfen, O. Paris, R. M. Wilson, F. C. Meldrum, *J. Am. Chem. Soc.* **2007**, *129*, 3729–3736.
[35] D. M. Phillips, L. F. Drummy, D. G. Conrady, D. M. Fox, R. R. Naik, M. O. Stone, P. C. Trulove, H. C. De Long, R. A. Mantz, *J. Am. Chem. Soc.* **2004**, *126*, 14350–14351.